Atmos. Chem. Phys., 25, 6353–6364, 2025
https://doi.org/10.5194/acp-25-6353-2025

Atmospheric Chemistry and Physics
Open Access

Research article

The optical properties of the stratospheric aerosol layer perturbation of the Hunga Tonga–Hunga Ha'apai volcano eruption of 15 January 2022

Pasquale Sellitto[1,2], Redha Belhadji[1], Bernard Legras[3], Aurélien Podglajen[3], and Clair Duchamp[3]

[1]Univ Paris Est Creteil and Université de Paris, CNRS, LISA, 94010 Créteil, France
[2]Istituto Nazionale di Geofisica e Vulcanologia, Osservatorio Etneo, Catania, Italy
[3]Laboratoire de Météorologie Dynamique (LMD-IPSL), CNRS, Sorbonne Université, ENS-PSL, École Polytechnique, Paris, France

Correspondence: Pasquale Sellitto (pasquale.sellitto@lisa.ipsl.fr)

Received: 14 May 2024 – Discussion started: 3 July 2024
Revised: 20 March 2025 – Accepted: 29 March 2025 – Published: 26 June 2025

Abstract. The Hunga Tonga–Hunga Ha'apai volcano violently erupted on 15 January 2022 and produced the largest stratospheric aerosol layer perturbation of the last 30 years. In comparison to background conditions and other recent moderate stratospheric eruptions, one notable effect of the Hunga Tonga–Hunga Ha'apai eruption was the significant modification of the size distribution (SD) of the stratospheric aerosol layer, resulting in a larger mean particle size and a smaller SD spread for Hunga Tonga–Hunga Ha'apai. Starting from satellite-based SD retrievals and the assumption of pure sulfate aerosol layers, in this work, we calculate the optical properties of both background and Hunga Tonga–Hunga Ha'apai-perturbed stratospheric aerosol scenarios using a Mie code. We found that the intensive optical properties of the stratospheric aerosol layer (i.e. the single-scattering albedo (SSA), the asymmetry parameter, the aerosol extinction per unit mass, and the broad-band average ultraviolet–visible (UV–Vis) to mid-infrared (MIR) Ångström exponent (AE)) were not significantly perturbed by the Hunga Tonga–Hunga Ha'apai eruption with respect to background conditions. The calculated AE was found to be consistent with multi-instrument satellite observations of the same parameter. Thus, the basic impact of the Hunga Tonga–Hunga Ha'apai eruption on the optical properties of the stratospheric aerosol layer was an increase in the stratospheric aerosol extinction (or optical depth), without any modification of the shortwave (SW) and longwave (LW) relative absorption, angular scattering, and broad-band spectral trend of the extinction, with respect to background. This highlights a marked difference between the Hunga Tonga–Hunga Ha'apai perturbation of the stratospheric aerosol layer and perturbations from other larger stratospheric eruptions, such as Pinatubo 1991 and El Chichón 1982. With simplified radiative forcing estimations, we show that the Hunga Tonga–Hunga Ha'apai eruption produced an aerosol layer likely 1.5–10 times more effective in producing a net cooling of the climate system with respect to the Pinatubo and El Chichón eruptions due to more effective SW scattering. As intensive optical properties are seldom directly measured, e.g. from satellite, our calculations can support the estimation of radiative effects for the Hunga Tonga–Hunga Ha'apai eruption with climate or offline radiative models.

1 Introduction

The Hunga Tonga–Hunga Ha'apai volcano (Kingdom of Tonga; 20.54° S, 175.38° W) violently erupted on 15 January 2022. Due to its very specific shallow submarine volcanological setting and the subsequent interaction of seawater with the volcanic magma chamber, this eruption was characterised by a large explosivity (e.g. Poli and Shapiro, 2022) and injected volcanic material at altitudes as large as 56 km, well into the deep stratosphere, with parts up to the lower mesosphere (Carr et al., 2022). Based on a wide array of satellite, ground-based, and in situ measurements, it was demonstrated that the Hunga Tonga–Hunga Ha'apai eruption produced the largest perturbation of the global stratospheric aerosol layer since the eruption of Mount Pinatubo (Philippines) in 1991 and the largest perturbation of stratospheric water vapour ever observed (Khaykin et al., 2022; Millán et al., 2022; Sellitto et al., 2022b; Vömel et al., 2022). An uncommonly fast conversion of volcanic sulfur dioxide (SO_2) emissions to sulfate aerosol (SA) was observed, with e-folding time from a few days to about 2 weeks (e.g. Carn et al., 2022; Asher et al., 2023; Sellitto et al., 2024). This was explained by the gas-to-particle kinetics acceleration due to very large water vapour concentrations through modelling studies (Zhu et al., 2022). Thus, these very specific perturbations are likely due to the exotic environment for the perturbed stratosphere and drove peculiar chemical and microphysical evolution within the Hunga Tonga–Hunga Ha'apai plume. The Hunga Tonga–Hunga Ha'apai stratospheric aerosol was quickly transported meridionally (timescales of weeks to months), and stratospheric aerosol perturbations were soon observed encompassing the whole Southern Hemisphere (Legras et al., 2022; Taha et al., 2022). The Hunga Tonga–Hunga Ha'apai aerosol layer showed an optical signature of ash for only a few days after the eruption (Sellitto et al., 2022b). Ash was likely removed from the stratosphere very quickly, and its optical signature was not observed after this transient period (Legras et al., 2022; Sellitto et al., 2022b). The Hunga Tonga–Hunga Ha'apai stratospheric aerosol perturbation can then solely be associated to SA. These effects proved long-lasting, with significantly perturbed aerosol extinctions extending well into the years 2022 and 2023 (Duchamp et al., 2023; Sellitto et al., 2024) and probably also into 2024. Using solar occultation satellite observations, Duchamp et al. (2023) observed aerosol size distributions (SDs) in the stratosphere that were significantly different to the usual volcanic perturbations for moderate stratospheric eruptions and the background stratospheric aerosol layer, with significantly larger mean radii and smaller widths of the aerosol SD. The liquid droplet nature and the relatively large mean size of the Hunga Tonga–Hunga Ha'apai aerosol particles were also confirmed with in situ balloon-borne optical counter measurements (Kloss et al., 2022). The aerosol perturbations due to the Hunga Tonga–Hunga Ha'apai eruption are associated with a larger stratospheric aerosol extinction per unit emitted SO_2 mass than recent major eruptions, such as the one of Pinatubo in 1991, due to the specific aerosol SD in the Hunga Tonga–Hunga Ha'apai plume and the high-altitude SO_2 injection (Li et al., 2024). In the absence of volcanic or other perturbations, a local maximum of the vertical aerosol distribution is found in the lower stratosphere, due to the troposphere-to-stratosphere exchange flux in sulfur-containing aerosol precursors at low latitudes and a very limited aerosol sink at these altitudes (Kremser et al., 2016; Norgren et al., 2024). Thus, a background stratospheric aerosol layer can be defined in the absence of episodic perturbation of this layer, i.e. stratospheric volcanic eruptions and pyro-convective fires. Secondary SA largely dominates the composition of the background aerosol layer (Kremser et al., 2016). The stratospheric aerosol layer perturbations induced by the Hunga Tonga–Hunga Ha'apai eruption are expected to have an impact on the optical properties of the stratospheric aerosol layer and on the Earth radiative balance, producing radiative and climatic impacts (Sellitto et al., 2022b).

In this paper, we use the SD determined by Duchamp et al. (2023) for both the Hunga Tonga–Hunga Ha'apai-perturbed and the background stratospheric aerosol layer, and we derive their optical properties. These optical properties and their possible effects on the radiative balance are then compared with those from the major recent eruptions, El Chichón in 1982 and Pinatubo in 1991. Our results are expected to contribute to the new estimations of the radiative forcing (RF) of the Hunga Tonga–Hunga Ha'apai eruption, which are presently ongoing to characterise the long-term radiative impacts of this event. This paper is structured as follows: in Sect. 2, the data and methods used in the paper are described; in Sect. 3, results are shown and discussed; conclusions are drawn in Sect. 4.

2 Data and methods

2.1 Chemical composition and refractive index

As discussed in the Introduction, both the background stratospheric aerosol layer and its perturbation brought by the Hunga Tonga–Hunga Ha'apai eruption can be solely characterised, in terms of composition, as secondary SA particles. Thus, we model both the background and Hunga Tonga–Hunga Ha'apai-perturbed stratospheric aerosol layers as composed of SA. These particles are usually represented as spherical liquid droplets of binary aqueous solution of sulfuric acid (H_2SO_4) as done by e.g. Sellitto and Legras (2016). The link between the chemical composition and the optical properties of a specific aerosol particle is provided by the complex refractive index (CRI). Among the available laboratory measurements of SA CRI, we have selected, for this work, the one from Hummel et al. (1988). This is one of the few datasets that extend the CRI spectra in both the shortwave (SW) and the longwave (LW) spectral ranges, from the ultraviolet (UV) to part of the far infrared (FIR), for representative stratospheric conditions in terms of the H_2SO_4 mass mixing ratio and temperature. Both the background stratospheric SA (e.g. Kremser et al., 2016) and the Hunga Tonga–Hunga Ha'apai perturbations (Duchamp et al., 2023) are characterised by very acidic particles with a H_2SO_4 mass mixing ratio of typically 70 %–80 %. Thus, a 75 % H_2SO_4 mixing ratio is selected in this work. Among the available particle temperatures in the Hummel et al. (1988) database, a temperature of 215 K is selected as the most suitable to represent lower- and mid-stratospheric conditions. Real and imaginary parts of CRI used in this work are shown in Fig. 1.

2.2 Size distribution

The number density SD $n(r)$ is defined so that $n(r)\mathrm{d}r$ is the number of particles per unit volume, in the aerosol layer, with a radius between r and $r+\mathrm{d}r$. All SDs in this work are modelled as mono-modal log-normal distributions (Eq. 1). In Eq. (1), N_0 is the total number concentration (in particles cm^{-3}); r_m is the median radius; and $S=\ln\sigma$ is the SD spread, i.e. the unitless standard deviation of $\ln(r/r_\mathrm{m})$.

$$n(r)=\frac{N_0}{r\ln\sigma\sqrt{2\pi}}e^{\frac{-1}{2}\left(\frac{\ln\left(\frac{r}{r_\mathrm{m}}\right)}{\ln\sigma}\right)^2} \tag{1}$$

Both background and Hunga Tonga–Hunga Ha'apai-perturbed typical SDs are derived from the results of Duchamp et al. (2023). In that work, SD parameters of a mono-modal log-normal SD, i.e. N_0, r_m, and σ in Eq. (1), are obtained using Stratospheric Aerosol and Gas Experiment III on the International Space Station (SAGE III/ISS) satellite observations with the method initially developed by Wrana et al. (2021). Duchamp et al. (2023) applied that method to the Hunga Tonga–Hunga Ha'apai plume and extended these retrievals back to immediate previously unperturbed periods, so as to also derive SD parameters for a representative background stratospheric aerosol layer. It is usually convenient, in remote sensing applications, to define an effective radius r_e (the cube particle radius divided by the square particle radius, averaged over the SD); r_e is directly linked to the extinction of the aerosol layer. For a mono-modal log-normal SD, an effective radius can be defined as $r_\mathrm{e}=r_\mathrm{m}e^{2.5\ln^2\sigma}$. For the background stratospheric aerosol layer, a typical combination of $r_\mathrm{m}=0.20\,\mu\mathrm{m}$ and $\sigma=1.50$ is considered (Fig. 2a and Table 1). The Hunga Tonga–Hunga Ha'apai eruption produced an increase in the mean particle size and a decrease in the spread of the particle SD with respect to background conditions (Duchamp et al., 2023). Typical values of Hunga Tonga–Hunga Ha'apai-perturbed stratospheric aerosol layers are used here, with r_e varying between 0.35 and 0.45 µm and σ varying between 1.20 and 1.30 (Fig. 2a and Table 1). In Fig. 2, N_0 is fixed to 1 particle cm^{-3} for the background and all Hunga Tonga–Hunga Ha'apai cases. As a further comparison, the Mount Pinatubo (Philippines) and El Chichón (Mexico) eruptions in 1991 and 1982 are also considered (Fig. 2b and Table 1). For the Pinatubo eruption, we use aerosol SD for both a relatively young plume (Asano, 1993) and an extreme case of an aged plume, i.e. several months after the eruption (Russell et al., 1996). Immediately after the Pinatubo eruption, the stratospheric aerosol perturbation was associated with relatively large particles (up to $r_\mathrm{m}=0.6\,\mu\mathrm{m}$) on average, with an extremely small SD width (down to $\sigma=1.05$) (Asano, 1993). The effective radius of the Pinatubo-perturbed aerosol layer increased during the first year after the eruption (extreme values as large as $r_\mathrm{e}=0.9\,\mu\mathrm{m}$) and then decreased slowly to background levels (Russell et al., 1996). Thus, the SDs used in this work for Pinatubo perturbation are to be regarded as two extreme values for this event. For the El Chichón eruption, only a small amount of information is available for the SD and its temporal evolution. In this paper, we consider the results of Hofmann and Rosen (1983), which are representative of the aerosol SD after about 1.5 months after the eruption of El Chichón.

Table 1. Parameters r_m, r_e, σ, and M_e for the SD in Fig. 2 for the background and Hunga Tonga–Hunga Ha'apai-perturbed stratospheric aerosol layers used in this paper and for the Mount Pinatubo-perturbed (two cases: early plume and aged plume) and El Chichón-perturbed (blue curve) SDs. All SDs in Fig. 2 are for a value of $N_0=1$ particles cm^{-3}. In the table, N_0 values for each SD are also reported, in the case of a fixed $M_\mathrm{e}=1\,\mu\mathrm{g\,m}^{-3}$ (last column).

r_m (µm)	r_e (µm)	σ	M_e ($\mu\mathrm{g\,m}^{-3}$)	N_0 (particles cm^{-3})
Background				
0.20	0.30	1.50	0.12	8.27
Hunga Tonga–Hunga Ha'apai-perturbed				
0.32	0.35	1.20	0.28	3.52
0.31	0.35	1.25	0.27	3.69
0.28	0.35	1.30	0.26	3.91
0.37	0.40	1.20	0.42	2.36
0.35	0.40	1.25	0.40	2.47
0.34	0.40	1.30	0.38	2.62
0.41	0.45	1.20	0.60	1.65
0.40	0.45	1.25	0.55	1.74
0.38	0.45	1.30	0.54	1.84
Pinatubo-perturbed, young plume (Asano, 1993)				
0.60	0.60	1.05	–	0.64
Pinatubo-perturbed, aged plume (Russell et al., 1996)				
0.60	0.90	1.50		0.31
El Chichón-perturbed (Hofmann and Rosen, 1983)				
0.72	1.71	1.80	–	0.08

For an SA layer of given mono-modal log-normal SD, the effective SA mass M_e (i.e. the total aerosol mass per unit volume in the layer) can be calculated as done in Eq. (2), where ρ is the mass density of SA (here taken as $1.75\,\mathrm{g\,cm}^{-3}$)

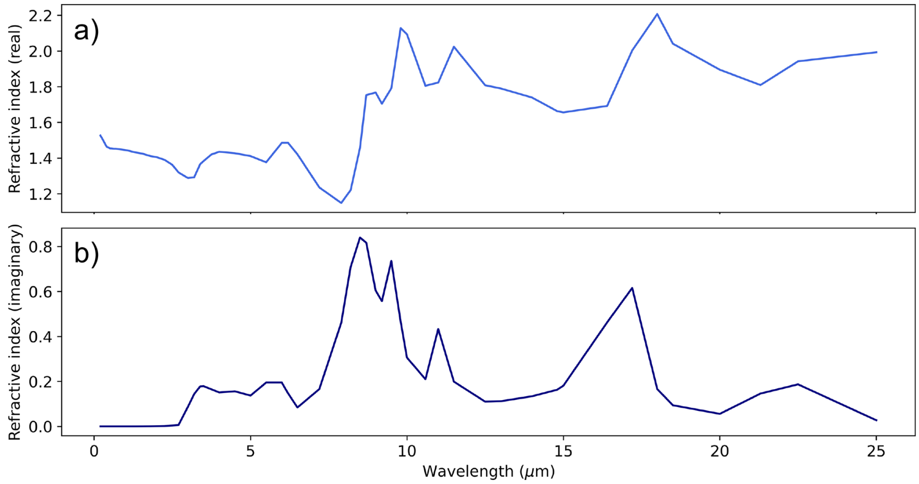

Figure 1. Real **(a)** and imaginary **(b)** parts of the complex refractive index of an SA layer with a mass mixing ratio of 75 % H_2SO_4 and a temperature of 215 K, from Hummel et al. (1988).

and $N_\mathrm{e} = N_0 e^{-3\ln^2\sigma}$ is the mono-modal log-normal effective number density. The M_e values for the SDs used in the present work are also indicated in Table 1.

$$M_\mathrm{e} = \frac{4}{3}\pi r_\mathrm{e}^3 \rho N_\mathrm{e} \quad (2)$$

2.3 Calculation of optical properties

The optical properties of background, Hunga Tonga–Hunga Ha'apai-perturbed, El Chichón-perturbed, and Pinatubo-perturbed stratospheric aerosol layers are calculated with the scheme shown in Fig. 3. Starting from CRI and SD input data described in Sect. 2.1 and 2.2, a Mie code estimates the extinction coefficient (β_ext), single-scattering albedo (SSA), and asymmetry parameter (g) spectra for both cases and for Mount Pinatubo (young and aged plume) and El Chichón as a further comparison. As Mie code, the Interactive Data Language (IDL; https://www.nv5geospatialsoftware.com/Products/IDL, last access: 18 June 2025) Mie-scattering routines of the Earth Observation Data Group of the Department of Physics of Oxford University are used (https://eodg.atm.ox.ac.uk/MIE/, last access: 18 June 2025). The outputs of the Mie calculations are intended to represent the overall extinction of typical stratospheric background and volcanically perturbed layers, along with their absorption/scattering properties (through SSA) and angular distribution of the scattered radiation (through g). The SSA is the ratio of the aerosol scattering to the aerosol extinction (i.e. scattering plus absorption) efficiency factors Q_sca and Q_ext obtained with Mie calculations (van de Hulst, 1957). Values of the SSA approaching 1.0 point towards pure scattering particles, while values of the SSA approaching 0.0 point towards pure absorbing particles. The g parameter is the mean value of the cosine of the scattering angle weighted though the scattering phase function obtained with Mie calculations (van de Hulst, 1957). Values of the g parameter approaching 1.0 point towards pure forward scattering, while values of the g parameter approaching 0.0 may point towards isotropic scattering. The overall extinction of the layers, measured by β_ext, is calculated with two different assumptions: a fixed N_0 and a fixed M_e. With the latter, extinction spectra per unit mass concentration ($\beta_\mathrm{ext}/M_\mathrm{e}$) are also derived. The SSA, g, and $\beta_\mathrm{ext}/M_\mathrm{e}$ are intensive optical properties of the aerosol layer; i.e. they do not depend on the injected aerosol mass. It was discussed previously that these optical parameters, together with surface reflectivity information fed to a radiative transfer model (RTM), are sufficient to describe the radiative properties and impacts of an aerosol layer, like the instantaneous radiative forcing and the vertical profiles of radiative/cooling heating rates (e.g. Sellitto et al., 2022a, 2023). In this work, optical properties in both the solar shortwave (SW) and the terrestrial longwave (LW) spectral ranges are estimated in order to produce results usable in RTMs when there is interest in the whole radiant energy spectrum in Earth's atmosphere. The output spectral range of the optical properties is somewhat limited by the available spectral range of the input CRI. In our case, we are limited at 25 µm on the upper end, due to available SA CRIs in the literature, so a part of the far-infrared range is not represented in this work, likely leading to an underestimation of its impact.

3 Results and discussion

3.1 Impact of size distribution on the optical properties

Figure 4 shows β_ext/N_0 and $\beta_\mathrm{ext}/M_\mathrm{e}$ calculation for the background and Hunga Tonga–Hunga Ha'apai-perturbed scenarios, as described in Sect. 2. The extinction is an extensive optical property that depends on the aerosol layer mass (the SA mass, in the present case). Thus,

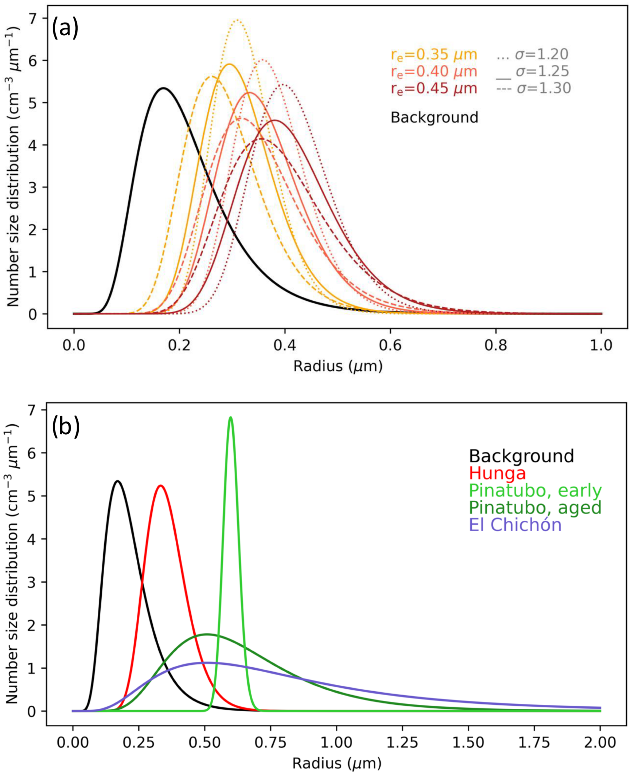

Figure 2. Typical background (black curve) and Hunga Tonga–Hunga Ha'apai-perturbed SDs (yellow, red, and dark-red curves) modelled as mono-modal log-normal SDs, with r_e and σ estimated using SAGE III/ISS by Duchamp et al. (2023) **(a)**. Background (black curve), Hunga Tonga–Hunga Ha'apai-perturbed (red curve; case for $r_e = 0.40\,\mu$m and $\sigma = 1.25$), Mount Pinatubo-perturbed (two cases: early plume, light-green curve; aged plume, dark-green curve), and El Chichón-perturbed SD (blue curve) **(b)**. Log-normal parameters for Pinatubo (young and aged plumes) and El Chichón SDs are taken from Asano (1993), Russell et al. (1996), and Hofmann and Rosen (1983), respectively. See Table 1 for more details on the SD parameters of all cases shown in the figure. Please note the different x-axis intervals in panels **(a)** and **(b)**.

large differences in β_{ext}/N_0 among background and Hunga Tonga–Hunga Ha'apai-perturbed scenarios can be observed (Fig. 4a). This is principally due to the larger SA mass, for a fixed number density $N_0 = 1.0$ particle cm^{-3}, of the larger Hunga Tonga–Hunga Ha'apai particles with respect to the smaller background particles. The effective mass varies from 0.12 µg cm^{-3} for the background layer to up to 0.60 µg cm^{-3} for the Hunga Tonga–Hunga Ha'apai-perturbed layers (see Table 1). On the contrary, β_{ext}/M_e is much less variable depending on the scenario, except at very short wavelengths in the SW (Fig. 4b). In general, a clear exponential decrease in β_{ext} can be observed in the UV–Vis and part of the near infrared (NIR), thus in most of the SW spectral range, following the empirical Ångström law in Eq. (3), where λ is the wavelength (λ_{ref} is a reference wavelength, in many cases taken as 1 µm) and AE is the Ångström exponent.

$$\beta_{ext}(\lambda) = \beta_{ext}(\lambda_{ref})\lambda^{-AE} \tag{3}$$

At longer wavelengths, absorption features of SA particles appear, including the peculiar mid-infrared (MIR) signatures at 8.0 to 11.0 µm. These absorption features can be associated with the rotational–vibrational absorption bands of the undissociated H_2SO_4 in the concentrated solution droplets discussed by e.g. Sellitto and Legras (2016). More absorption features are visible in the NIR, from about 3.0 to 6.0 µm, and in the FIR, from 15.0 to 18.0 µm. The two regimes, dominated by scattering in the SW for wavelengths shorter than about 3.0 µm and by absorption in the LW for longer wavelengths, are discussed further in the following (associated with SSA) and are linked to a large variability in β_{ext}/M_e. The latter ranges between less than 1.0×10^{-3} km^{-1} per unit effective mass above 3.0 µm and 4.5×10^{-3} km^{-1} per unit effective mass below 3.0 µm.

Figure 5 shows the SSA (Fig. 5a) and g (Fig. 5b) calculations for the background and Hunga Tonga–Hunga Ha'apai-perturbed scenarios. The first takeaway message from these results is that both SSA and g are not significantly perturbed by the Hunga Tonga–Hunga Ha'apai eruption and that their absolute values and variability are similar for background and Hunga Tonga–Hunga Ha'apai-perturbed scenarios. The two scattering- and absorption-dominated regimes, discussed for the aerosol extinction, can be seen here with an SSA of approximately 1.0 (pure scattering aerosol layers) for wavelengths shorter than about 3.0 µm, sharply decreasing to values lower than about 0.2 for wavelengths longer than about 3.0 µm. The SSA approaches values of 0.0 (pure absorbing particles) for wavelengths longer than about 6.0 µm. The g parameter, starting from values of about 0.6 to 0.8, steeply decreases to values lower than 0.1 for wavelengths longer than 6.0 µm. This can be associated with a markedly dominating forward scattering in the SW and a quasi-isotropic scattering in the LW. Figures 4 and 5 are also shown on a vertical log-scale in Fig. S1 in the Supplement.

These results are summarised in Fig. 6, where spectral band average values of the intensive optical properties β_{ext}/M_e, SSA, and g, for background and Hunga Tonga–Hunga Ha'apai-perturbed layers, are shown for the UV–Vis, NIR, MIR, and FIR broad-band ranges. Large values for the three intensive parameters are found in the UV–Vis, thus pointing towards very extinction-effective layers dominated by a largely forward scattering. While this characteristic behaviour of the aerosol layers stands for the whole SW, the extinction efficiency markedly decreases in the NIR. In the LW, the optical characterisation of the layers is more spectrally homogeneous, with relatively small extinction dominated by absorption and a small quasi-isotropic scattering, with small differences between the MIR and the FIR.

More generally, the most apparent effect, visible in Figs. 4–6, is that all intensive optical properties of the Hunga

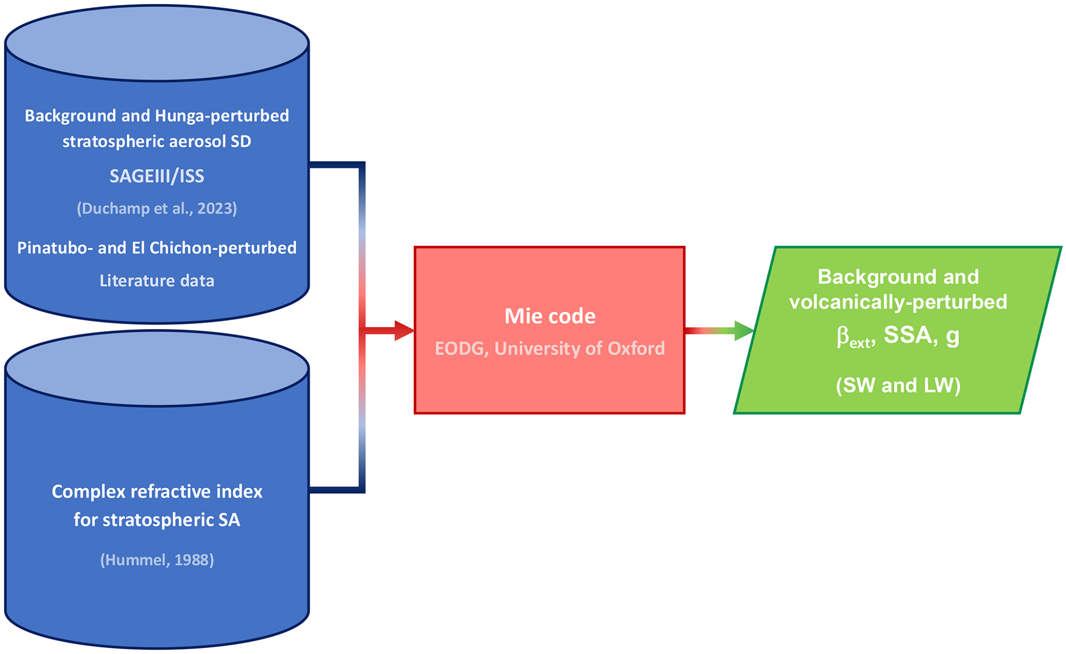

Figure 3. Schematic of the calculations of optical properties used in this work.

Tonga–Hunga Ha'apai-perturbed layer are very similar to those in background conditions. It can be concluded that, despite the significant perturbation in stratospheric aerosol SD and the relatively large mass of the injected SA, the Hunga Tonga–Hunga Ha'apai eruption had minimal effects on the intensive optical properties of the stratospheric aerosol layer. Thus, the only impact of the Hunga Tonga–Hunga Ha'apai eruption on the optical properties of the stratospheric aerosol layer is the marked increase in the overall extinction and the aerosol optical depth (AOD). For this latter property, Hunga Tonga–Hunga Ha'apai produced the largest global perturbation since the Mount Pinatubo eruption in 1991 (Sellitto et al., 2022b). The specific absorption and scattering properties of the stratospheric aerosol layer were not significantly perturbed in the SW and LW by the Hunga Tonga–Hunga Ha'apai eruption, as shown by the SSA and g calculations of Figs. 5 and 6b, c. It must be noted that Hunga Tonga–Hunga Ha'apai perturbations on the stratospheric aerosol SD, though significant, are much smaller than for other, stronger recent eruptions, such as El Chichón in 1982 (Hofmann and Rosen, 1983) or the aged Pinatubo in 1991 (e.g. Russell et al., 1996); see respective SDs in Fig. 2b. In these cases, a fraction of relatively large particles (larger than 1.0 µm) was present, which is not the case for the Hunga Tonga–Hunga Ha'apai eruption (see Fig. 2b). For the fresh Pinatubo plume, i.e. during the first few months after the eruption in 1991, larger particles were present, on average, than for the Hunga Tonga–Hunga Ha'apai eruption, but with a minimal contribution of particles larger than 1.0 µm, due to the exceptionally small width of its SD (Asano, 1993). We performed additional Mie calculations for the Pinatubo and El Chichón SDs, using the SD parameters of Asano (1993), Russell et al. (1996), and Hofmann and Rosen (1983), summarised in Table 1. For the aged Pinatubo and El Chichón cases, the UV–Vis β_{ext}/M_e is significantly smaller, and the overall LW SSA and g are significantly larger, than for Hunga Tonga–Hunga Ha'apai and the stratospheric background (Fig. 6). This effect, even if still present, is less strong for the fresh Pinatubo plume. Such a change in optical regime implies a stronger LW climate warning effect that can counterbalance the SW cooling. More generally, Lacis et al. (1992) showed that a marked change in optical and radiative regime occurs for volcanic aerosol layers with mean size exceeding 1.0 µm, which is the case for the aged Pinatubo plume and El Chichón but not for the Hunga Tonga–Hunga Ha'apai perturbations. This change in the SW / LW optical properties can result in less effective cooling at top of the atmosphere or even in aerosol-related warming, which could initially have been the case for the Pinatubo and El Chichón eruptions (before a marked and relatively long-term cooling effect due to the removal of larger aerosol particles) but was likely not the case for Hunga Tonga–Hunga Ha'apai, even in the first phases after the eruption (e.g. Sellitto et al., 2022b). The mean particle size for Hunga Tonga–Hunga Ha'apai was larger than any post-Pinatubo stratospheric eruption (Wrana et al., 2023). Most post-Pinatubo eruptions perturbed the stratospheric aerosol layer with a decrease in mean particle size, rather than an increase. The radiative effects of the Hunga Tonga–Hunga Ha'apai-related aerosol SD perturbations are discussed more in Sect. 3.2.

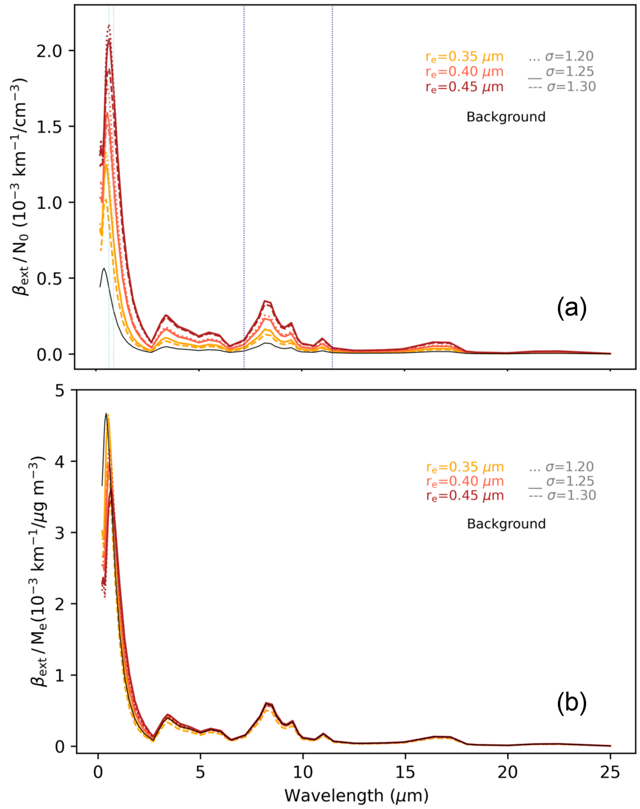

Figure 4. Extinction coefficient spectra β_{ext} at fixed number concentration N_0 **(a)** and effective mass M_e **(b)** for background (black curve) and Hunga Tonga–Hunga Ha'apai-perturbed aerosol layers (from yellow, red, and dark-red dotted, dashed, and solid curves; see corresponding values of the r_e and σ assumption in the figure captions). The light- and dark-blue vertical dotted lines in panel **(a)** indicate the two wavelength bands (UV–Vis and MIR, respectively) used to average the extinction to calculate the UV–Vis to MIR AE of Fig. 7.

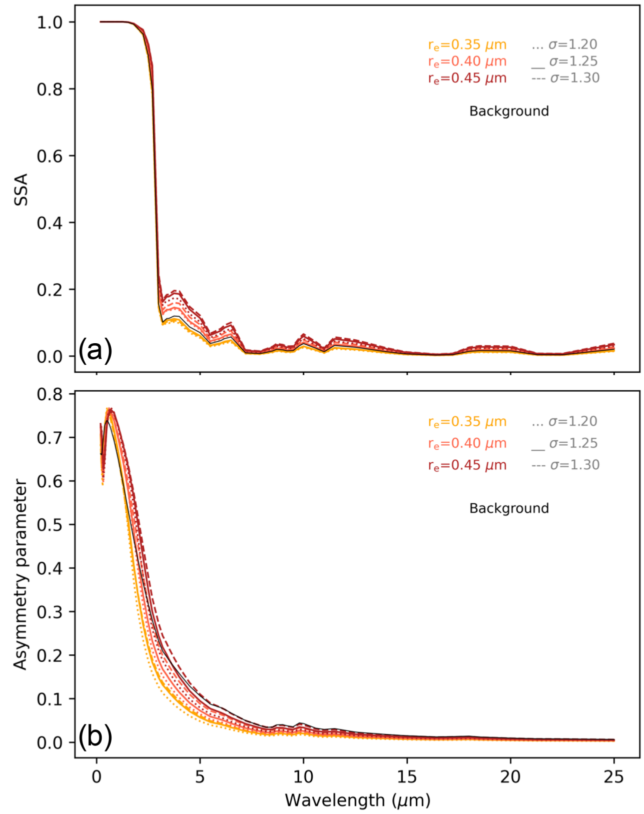

Figure 5. Same as Fig. 4 but for single-scattering albedo (SSA) **(a)** and asymmetry parameter (g) **(b)** spectra.

Another intensive aerosol optical parameter is the Ångström exponent (AE); see also Eq. (3). An average AE can be obtained by combining aerosol extinction or AOD information at two different wavelengths. In Sellitto et al. (2024), the average UV–Vis to MIR AE was calculated using combination of Ozone Mapping and Profiler Suite Limb Profiler (OMPS LP) and Infrared Atmospheric Sounding Interferometer (IASI) observations at 0.7 and 8.5 µm, respectively. As for other intensive optical properties shown above, the stratospheric aerosol layer UV–Vis to MIR AE obtained using our calculations is not significantly perturbed by the Hunga Tonga–Hunga Ha'apai eruption, and background and Hunga Tonga–Hunga Ha'apai-perturbed values stay around a value of 1.0 (0.94 for the background stratospheric conditions and 0.97 ± 0.02 for Hunga Tonga–Hunga Ha'apai-perturbed conditions, with standard deviation representing the variability associated with the different Hunga Tonga–Hunga Ha'apai SDs). These results are not dissimilar to the observed value (1.13 ± 0.23), even if $\sim 15\,\%$ smaller. Thus, this shows the consistency of our calculated optical properties and the observed optical properties for the Hunga Tonga–Hunga Ha'apai plume. It has to be noted that Taha et al. (2022) showed that the observed Vis AE, i.e. estimated with two different Vis bands of the OMPS LP instrument (0.52 and 1.02 µm), is significantly perturbed by the Hunga Tonga–Hunga Ha'apai eruption. The AE estimation from observations is very sensitive to the selection of the two wavelengths used to derive it. Using the same wavelengths as in Taha et al. (2022), we obtain a Vis AE of 1.35 and 0.80 for the background and Hunga Tonga–Hunga Ha'apai-perturbed scenarios. This is very consistent with past theoretical studies, i.e. the one of Schuster et al. (2006) (see their Fig. 4a, with effective radii 0.30 µm and 0.40–0.45 µm, respectively). The variability in the UV–Vis AE, in terms of the selected background or Hunga Tonga–Hunga Ha'apai-perturbed scenarios, can also be seen in Fig. 4, reflected by the different slopes of the spectral variability in the extinction coefficient.

3.2 Impact of optical properties on the radiative forcing

A simple parameterisation of the top-of-atmosphere (TOA) radiative forcing is used to estimate the radiative impact, through the perturbation of the optical properties, of the

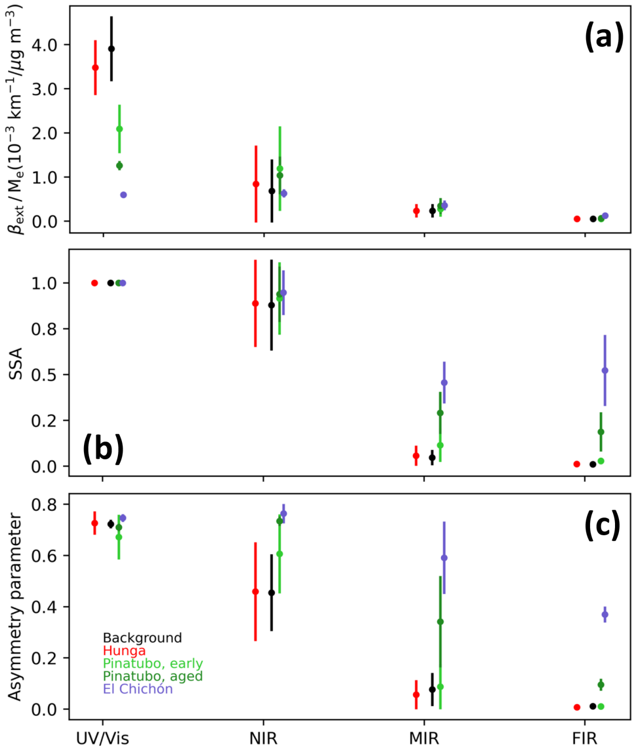

Figure 6. Band average (UV–Vis, NIR, MIR, and FIR) extinction coefficient per unit effective mass **(a)**, single-scattering albedo **(b)**, and asymmetry parameter **(c)** for the background (black circles with error bars) and Hunga Tonga–Hunga Ha'apai-perturbed (averaged over all scenarios in e.g. Fig. 2; red circles with error bars) stratospheric aerosol layers. Band average values of these intensive aerosol optical properties are also shown for Pinatubo (two cases: early plume, light-green circles with error bars; aged plume, dark-green circles with error bars) and El Chichón (blue circles with error bars). UV–Vis (ultraviolet–visible): 0.30–0.85 mm; NIR (near infrared): 0.85–3.0 mm; MIR (mid-infrared): 3.0–15.0 mm; FIR (far infrared): 15.0–25.0 mm.

modification of the SD of stratospheric aerosol by the Hunga Tonga–Hunga Ha'apai eruption. For partly absorbing aerosols in a layer over a given surface of spectral reflectivity R_s and placed in a stratified atmosphere of spectral transmissivity T_{atm}, a broad-band TOA radiative forcing ΔF per unit SA mass can be defined as in Eq. (4). This quantity is estimated at the four broad-band spectral ranges, as defined in e.g. Fig. 6 (UV–Vis, NIR, MIR, and FIR), then these broad-band estimations are added up to obtain a total ΔF. In Eq. (4), the optical properties β_{ext}/M_e and SSA are the same as in Fig. 6. The optical parameter b is the hemispheric backscatter ratio, which can be derived using our asymmetry parameter g estimations, using the method described by Marshall et al. (1995). The aerosols are put in a 1 km deep layer. In the parameterisation, S is the radiation source, taken as pure Planck functions at temperatures of 5770 K in the SW range (UV–Vis and NIR broad bands) and 300 K in the LW range (MIR and FIR broad bands), to simulate the solar and terrestrial radiation sources. The solar S component is then scaled at the mean Sun–Earth distance. The diurnal cycle of S was not considered in this example. The underlying surface is regarded as marine (R_s 0.05 in the UV–Vis and FIR; 0.00 in the NIR and MIR), and average values of T_{atm} are also considered (0.6, 0.5, 0.5, and 0.2 in the UV–Vis, NIR, MIR and FIR).

$$\Delta F = -S(\lambda)T_{atm}(\lambda)\frac{\beta_{ext}(\lambda)}{M_e}\mathrm{SSA}(\lambda)b(\lambda) \times \left((1-R_s(\lambda))^2 + 2R_s(\lambda)\left(\frac{1-\mathrm{SSA}(\lambda)}{b(\lambda)\mathrm{SSA}(\lambda)}\right)\right)\Delta\lambda \quad (4)$$

The SW (UV–Vis + NIR), LW (MIR + FIR), and total (SW + LW) radiative forcings obtained with Eq. (4) and our estimated optical parameters are shown in Fig. 7 for a background stratospheric aerosol layer and for layers perturbed by the Hunga Tonga–Hunga Ha'apai, Pinatubo, and El Chichón eruptions. Two different radiative regimes can be observed in Fig. 7. The first regime, for smaller effective radii, is clearly dominated by the SW scattering, thus resulting in a large negative radiative forcing per unit mass. The second regime, for larger effective radii, is less and less dominated by the decreasing SW scattering with increasing mean size and the progressively increasing importance of the LW warming effect due to the LW absorbing effect. In the latter case, the total radiative forcing per unit SA mass decreases significantly with respect to background conditions. In addition, the SW / LW absolute ratio of the ΔF is approximately 99 %, 98 %, 80 %, and 60 % for the background, Hunga Tonga–Hunga Ha'apai, aged Pinatubo, and El Chichón scenarios. These results point towards very different overall radiative regimes between the background and Hunga Tonga–Hunga Ha'apai with respect to aged Pinatubo and El Chichón. For the young Pinatubo plume, the SW / LW absolute ratio of the ΔF is around 90 %, larger than for the aged Pinatubo plume while still smaller than for the Hunga Tonga–Hunga Ha'apai-perturbed scenario. The Hunga Tonga–Hunga Ha'apai eruption did not significantly modify the radiative regime of the stratospheric aerosol layer with respect to background conditions, with values around $-0.17\,\mathrm{W\,m^{-2}}$ (μg m^{-3} SA)$^{-1}$, dominated by SW scattering (pink triangle in Fig. 7). This is 1.5 to 4 times more effective, per unit SA mass, than the Pinatubo eruption (about -0.12 to $-0.040\,\mathrm{W\,m^{-2}}$ (μg m^{-3} SA)$^{-1}$, depending on the ageing of the plume; pink squares in Fig. 7) and nearly 10 times more effective than the El Chichón eruption (about $-0.015\,\mathrm{W\,m^{-2}}$ (μg m^{-3} SA)$^{-1}$; pink hexagon in Fig. 7). For the latter, the SW cooling and the SW / LW ratio markedly decreased with respect to the background and the Hunga Tonga–Hunga Ha'apai eruption. Our results are consistent with previous studies, particularly the one of Lacis et al. (1992), who showed that the cooling potential at the TOA of stratospheric aerosols significantly decreases for effective

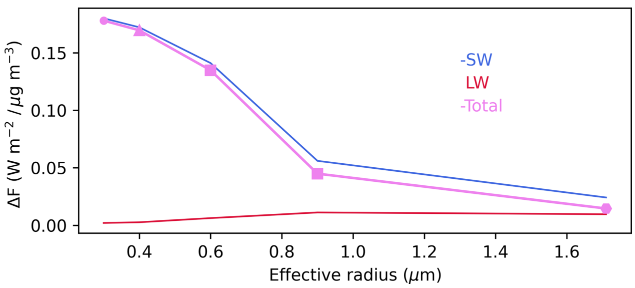

Figure 7. TOA RF (ΔF) in the SW (negative; dark-blue lines), LW (dark-red lines), and total SW + LW (negative; pink lines and symbols) as a function of the effective radius for background conditions (pink dot), Hunga Tonga–Hunga Ha'apai (pink triangle), Pinatubo (pink squares), and El Chichón (pink hexagon); see text for details.

radii larger than about 1.0 µm and can even switch from negative (cooling) to positive (warming) for effective radii larger than 2.0 µm (see their Fig. 2). The effect of a significantly larger RF per unit SA mass, with respect to major recent eruptions, adds up with the larger stratospheric AOD production per unit SO_2 injected mass shown by Li et al. (2024). Thus, for different factors, including the high-altitude injection and the aerosol SD, the Hunga Tonga–Hunga Ha'apai eruption produced stratospheric aerosol perturbations with a particularly large potential to produce a negative RF and a cooling of the climate system. These factors can be associated with the phreatic nature of the eruption and therefore with the interaction with seawater before the eruption and the subsequent availability of water vapour in the plume. It is important to recall that the Hunga Tonga–Hunga Ha'apai eruption is characterised by much less injected SO_2 and SA mass than the Pinatubo and El Chichón eruptions, so, despite the larger radiative effectiveness of its stratospheric aerosol perturbations, in terms of the SD, its overall radiative effect is expected to be smaller than Pinatubo and El Chichón. The direct radiative effect of water vapour must also be considered. Water vapour can produce a warming at the TOA that can bias or revert the cooling effect of the sulfate aerosol layer (Sellitto et al., 2022b).

Optical properties of aerosol layers are needed, in radiative calculations with both climate models and offline radiative models, for a given source of radiative forcing to estimate its impacts (e.g. Sellitto et al., 2022a, 2023). Our results provide a ready-to-use benchmark for the radiative impact estimations of the Hunga Tonga–Hunga Ha'apai eruption versus stratospheric aerosol background. Thus, in the Supplement, we provide datasets on optical properties (1) computed at the wavelengths at which the refractive indices of Hummel et al. (1988) are available and (2) averaged over the 30 broad bands of the Rapid Radiative Transfer Model (RRTM; Iacono et al., 2008) in the ECMWF ECRAD implementation (Hogan and Bozzo, 2018) (the latter are provided as a netCDF file) for future studies on the Hunga Tonga–Hunga Ha'apai radiative impacts. Averaged values for the UV–Vis, NIR, MIR, and FIR bands are also reported in Table 2 (same as Fig. 6). Caution must be taken for the radiative impact estimation of the Hunga Tonga–Hunga Ha'apai eruption because of the additional important radiative impacts of water vapour injections, which can be even larger than aerosol impacts during the first months (Sellitto et al., 2022b). This additional radiative effect for the Hunga Tonga–Hunga Ha'apai eruption was not present in recent stratospheric volcanic eruptions from subaerial volcanoes.

4 Conclusions

The submarine Hunga Tonga–Hunga Ha'apai volcano violently erupted on 15 January 2022 and produced the largest stratospheric aerosol layer perturbation, in terms of the aerosol extinction and the injected aerosol mass, since the climate-relevant eruption of the Pinatubo volcano in 1991. One notable feature of this perturbation is the significant modification of the stratospheric aerosol SD, with larger particles (0.35–0.45 µm effective radius) and a smaller SD width (1.20–1.30 spread in a modelled mono-modal size distribution) compared to the background stratospheric aerosol layer and to most other post-Pinatubo stratospheric eruptions. In this paper, using a Mie code and the assumption of pure SA layers, we calculate the optical properties of the Hunga Tonga–Hunga Ha'apai-perturbed stratospheric aerosol layer and compare with those for a background scenario. We found that, despite the sensible impact on the aerosol SD, the Hunga Tonga–Hunga Ha'apai eruption had only a minor impact on the intensive optical properties, namely the aerosol extinction per unit effective mass (β_{ext}/M_e), the single-scattering albedo (SSA), the asymmetry parameter (g), and the broad-band UV–Vis to MIR Ångström exponent (AE). Thus, while producing a historical perturbation on the stratospheric aerosol extinction and optical depth, the Hunga Tonga–Hunga Ha'apai eruption did not modify the absorption and angular scattering properties of the stratospheric aerosol layer. Our UV–Vis to MIR AE calculations are consistent with those observed with the combination of OMPS LP and IASI satellite observations. We further calculate intensive aerosol optical properties for past eruptions of Pinatubo 1991 and El Chichón 1982 and found that these latter events produced enough particles with radii > 1 µm to change their SW / LW optical regimes with respect to stratospheric background, which was not the case for Hunga Tonga–Hunga Ha'apai. We demonstrate here, with a simplified radiative forcing parameterisation, that the Hunga Tonga–Hunga Ha'apai eruption has likely produced stratospheric aerosol layers with a cooling potential 1.5 to 10 times larger than the Pinatubo and El Chichón eruptions, due to different SD-related radiative regimes. Hunga Tonga–Hunga Ha'apai-related stratospheric aerosol perturbations are more effective

Table 2. Summary of band average ready-to-use optical property inputs for radiative calculations.

Spectral interval (µm)	Spectral interval acronym	AE background	SSA background	g background	AE Hunga Tonga–Hunga Ha'apai-perturbed	SSA Hunga Tonga–Hunga Ha'apai-perturbed	g Hunga Tonga–Hunga Ha'apai-perturbed
0.3–0.8	UV–Vis	0.94	0.99 ± 0.00	0.72 ± 0.02	0.97 ± 0.02	0.99 ± 0.00	0.73 ± 0.05
0.8–3.0	NIR		0.88 ± 0.25	0.45 ± 0.15		0.89 ± 0.24	0.46 ± 0.19
3.0–15.0	MIR		0.05 ± 0.04	0.08 ± 0.06		0.06 ± 0.06	0.06 ± 0.06
15.0–25.0	FIR		0.01 ± 0.01	0.01 ± 0.00		0.01 ± 0.01	0.01 ± 0.00

in SW cooling than Pinatubo- and El Chichón-related perturbations. Values as large as $-0.17\,\mathrm{W\,m^{-2}}\,(\mathrm{\mu g\,m^{-3}\,SA})^{-1}$ are found for the Hunga Tonga–Hunga Ha'apai eruption (as comparisons: for Pinatubo, values of -0.12 to $-0.040\,\mathrm{W\,m^{-2}}\,(\mathrm{\mu g\,m^{-3}\,SA})^{-1}$ are found; for El Chichón, values as small as $-0.015\,\mathrm{W\,m^{-2}}\,(\mathrm{\mu g\,m^{-3}\,SA})^{-1}$ are found). Our study highlights the importance of having detailed information on the aerosol SD to obtain reliable estimations of its radiative impacts. Our calculations of optical properties create a ready-to-use dataset for future estimations of the radiative impacts of the Hunga Tonga–Hunga Ha'apai eruption compared with background and combined with pertinent water vapour observations, another important forcing agent for this submarine eruption.

Data availability. The SA CRI data used in this work are freely available at the GEISA (Gestion et Etude des Informations Spectroscopiques Atmosphériques: Management and Study of Atmospheric Spectroscopic Information) web page: http://cds-espri.ipsl.fr/GEISA/AEROSOLS/geisaAerosols.php (AERIS, 2025).

Supplement. The supplement related to this article is available online at https://doi.org/10.5194/acp-25-6353-2025-supplement.

Author contributions. PS conceived and performed the study and wrote the first version of the article. All authors discussed the results and contributed to the final version of the article.

Competing interests. At least one of the (co-)authors is a member of the editorial board of *Atmospheric Chemistry and Physics*. The peer-review process was guided by an independent editor, and the authors also have no other competing interests to declare.

Acknowledgements. The optical properties used in this work are obtained with the IDL Mie-scattering routines developed by the Earth Observation Data Group of the Department of Physics of Oxford University and are available at http://eodg.atm.ox.ac.uk/MIE/ (last access: 18 June 2025).

Financial support. This research has been supported by the Centre National d'Etudes Spatiales (grant no. TOSCA/EXTRA-SAT) and the Agence Nationale de la Recherche (grant no. ASTuS).

Review statement. This paper was edited by Luis Millan and reviewed by three anonymous referees.

References

AERIS: GEISA: spectroscopic database, http://cds-espri.ipsl.fr/GEISA/AEROSOLS/geisaAerosols.php, last access: 18 June 2025.

Asano, S.: Estimation of the size distribution of Pinatubo volcanic dust from Bishop's ring simulations, Geophys. Res. Lett., 20, 447–450, https://doi.org/10.1029/93GL00512, 1993.

Asher, E., Todt, M., Rosenlof, K., Thornberry, T., Gao, R., Taha, G., Walter, P., Alvarez, S., Flynn, J., Davis, S. M., Evan, S., Brioude, J., Metzger, J., Hurst, D. F., Hall, E., and Xiong, K.: Unexpectedly rapid aerosol formation in the Hunga Tonga plume, P. Natl. Acad. Sci. USA, 120, e2219547120, https://doi.org/10.1073/pnas.2219547120, 2023.

Carn, S. A., Krotkov, N. A., Fisher, B. L., and Li, C.: Out of the blue: Volcanic SO_2 emissions during the 2021–2022 eruptions of Hunga Tonga – Hunga Ha'apai (Tonga), Front. Earth Sci., 10, 976962, https://doi.org/10.3389/feart.2022.976962, 2022.

Carr, J. L., Horvath, A., Wu, D. L., and Friberg, M. D.: Stereo Plume Height and Motion Retrievals for the Record-Setting Hunga Tonga-Hunga Ha'apai Eruption of 15 January 2022, Geophys. Res. Lett., 49, e2022GL098131, https://doi.org/10.1029/2022GL098131, 2022.

Duchamp, C., Wrana, F., Legras, B., Sellitto, P., Belhadji, R., and von Savigny, C.: Observation of the aerosol plume from the 2022 Hunga Tonga – Hunga Ha'apai eruption with SAGE III/ISS, Geophys. Res. Lett., 50, e2023GL105076, https://doi.org/10.1029/2023GL105076, 2023.

Hofmann, D. J. and Rosen, J. M.: Sulfuric Acid Droplet Formation and Growth in the Stratosphere After the

1982 Eruption of El Chichón, Science, 222, 325–327, https://doi.org/10.1126/science.222.4621.325, 1983.

Hogan, R. J. and Bozzo, A.: A Flexible and Efficient Radiation Scheme for the ECMWF Model, J. Adv. Model. Earth Sy., 10, 1990–2008, https://doi.org/10.1029/2018MS001364, 2018.

Hummel, J. R., Shettle, E. P., and Longtin, D. R.: A new background stratospheric aerosol model for use in atmospheric radiation models, Tech. Rep., provided by the SAO/NASA Astrophysics Data System, https://ui.adsabs.harvard.edu/abs/1988nbsa.rept.....H (last access: 18 June 2025), 1988.

Iacono, M. J., Delamere, J. S., Mlawer, E. J., Shephard, M. W., Clough, S. A., and Collins, W. D.: Radiative forcing by long-lived greenhouse gases: Calculations with the AER radiative transfer models, J. Geophys. Res., 113, D13103, https://doi.org/10.1029/2008JD009944, 2008.

Khaykin, S., Podglajen, A., Ploeger, F., Grooß, J. U., Tence, F., Bekki, S., Khlopenkov, K., Bedka, K., Rieger, L., Baron, A., Godin-Beekmann, S., Legras, B., Sellitto, P., Sakai, T., Barnes, J., Uchino, O., Morino, I., Nagai, T., Wing, R., Baumgarten, G., Gerding, M., Duflot, V., Payen, G., Jumelet, J., Querel, R., Liley, B., Bourassa, A., Clouser, B., Feofilov, A., Hauchecorne, A., and Ravetta, F.: Global perturbation of stratospheric water and aerosol burden by Hunga eruption, Commun. Earth Environ., 3, 316, https://doi.org/10.1038/s43247-022-00652-x, 2022.

Kloss, C., Sellitto, P., Renard, J.-B., Baron, A., Bègue, N., Legras, B., Berthet, G., Briaud, E., Carboni, E., Duchamp, C., Duflot, V., Jacquet, P., Marquestaut, N., Metzger, J.-M., Payen, G., Ranaivombola, M., Roberts, T., Siddans, R., and Jégou, F.: Aerosol characterization of the stratospheric plume from the volcanic eruption at Hunga Tonga 15 January 2022, Geophys. Res. Lett., 49, e2022GL099394, https://doi.org/10.1029/2022GL099394, 2022.

Kremser, S., Thomason, L. W., von Hobe, M., Hermann, M., Deshler, T., Timmreck, C., Toohey, M., Stenke, A., Schwarz, J. P., Weigel, R., Fueglistaler, S., Prata, F. J., Vernier, J.-P., Schlager, H., Barnes, J. E., Antuña-Marrero, J.-C., Fairlie, D., Palm, M., Mahieu, E., Notholt, J., Rex, M., Bingen, C., Vanhellemont, F., Bourassa, A., Plane, J. M. C., Klocke, D., Carn, S. A., Clarisse, L., Trickl, T., Neely, R., James, A. D., Rieger, L., Wilson, J. C., and Meland, B.: Stratospheric aerosol—Observations, processes, and impact on climate, Rev. Geophys., 54, 278–335, https://doi.org/10.1002/2015RG000511, 2016.

Lacis, A., Hansen, J., and Sato, M.: Climate forcing by stratospheric aerosols, Geophys. Res. Lett., 19, 1607–1610, https://doi.org/10.1029/92GL01620, 1992.

Legras, B., Duchamp, C., Sellitto, P., Podglajen, A., Carboni, E., Siddans, R., Grooß, J.-U., Khaykin, S., and Ploeger, F.: The evolution and dynamics of the Hunga Tonga–Hunga Ha'apai sulfate aerosol plume in the stratosphere, Atmos. Chem. Phys., 22, 14957–14970, https://doi.org/10.5194/acp-22-14957-2022, 2022.

Li, C., Peng, Y., Asher, E., Baron, A. A., Todt, M., Thornberry, T. D., Evan, S., Brioude, J., Smale, P., Querel, R., Rosenlof, K. H., Zhou, L., Xu, J., Qie, K., Bian, J., Toon, O. B., Zhu, Y., and Yu, P.: Microphysical simulation of the 2022 Hunga volcano eruption using a sectional aerosol model, Geophys. Res. Lett., 51, e2024GL108522, https://doi.org/10.1029/2024GL108522, 2024.

Marshall, S. F., Covert, D. S., and Charlson, R. J.: Relationship between asymmetry parameter and hemispheric backscatter ratio: Implications for climate forcing by aerosols, Appl. Optics, 34, 63066311, https://doi.org/10.1364/AO.34.006306, 1995.

Millán, L., Santee, M. L., Lambert, A., Livesey, N. J., Werner, F., Schwartz, M. J., Pumphrey, H. C., Manney, G. L., Wang, Y., Su, H., Wu, L., Read, W. G., and Froidevaux, L.: The Hunga Tonga-Hunga Ha'apai hydration of the stratosphere, Geophys. Res. Lett., 49, e2022GL099381, https://doi.org/10.1029/2022GL099381, 2022.

Norgren, M., Kalnajs, L. E., and Deshler, T.: Measurements of total aerosol concentration in the stratosphere: A new balloon-borne instrument and a report on the existing measurement record, J. Geophys. Res.-Atmos., 129, e2024JD040992, https://doi.org/10.1029/2024JD040992, 2024.

Poli, P. and Shapiro, N. M.: Rapid Characterization of Large Volcanic Eruptions: Measuring the Impulse of the Hunga Tonga Ha'apai Explosion From Teleseismic Waves, Geophys. Res. Lett., 49, e2022GL098123, https://doi.org/10.1029/2022GL098123, 2022.

Russell, P. B., Livingston, J. M., Pueschel, R. F., Bauman, J. J., Pollack, J. B., Brooks, S. L., Hamill, P., Thomason, L. W., Stowe, L. L., Deshler, T., Dutton, E. G., and Bergstrom, R. W.: Global to microscale evolution of the Pinatubo volcanic aerosol derived from diverse measurements and analyses, J. Geophys. Res., 101, 18745–18763, https://doi.org/10.1029/96JD01162, 1996.

Schuster, G. L., Dubovik, O., and Holben, B. N.: Angstrom exponent and bimodal aerosol size distributions, J. Geophys. Res., 111, D07207, https://doi.org/10.1029/2005JD006328, 2006.

Sellitto, P. and Legras, B.: Sensitivity of thermal infrared nadir instruments to the chemical and microphysical properties of UTLS secondary sulfate aerosols, Atmos. Meas. Tech., 9, 115–132, https://doi.org/10.5194/amt-9-115-2016, 2016.

Sellitto, P., Belhadji, R., Kloss, C., and Legras, B.: Radiative impacts of the Australian bushfires 2019–2020 – Part 1: Large-scale radiative forcing, Atmos. Chem. Phys., 22, 9299–9311, https://doi.org/10.5194/acp-22-9299-2022, 2022a.

Sellitto, P., Podglajen, A., Belhadji, R., Boichu, M., Carboni, E., Cuesta, J., Duchamp, C., Kloss, C., Siddans, R., Bègue, N., Blarel, L., Jegou, F., Khaykin, S., Renard, J.-B., and Legras, B.: The unexpected radiative impact of the Hunga Tonga eruption of 15th January 2022, Comm. Earth Environ., 3, 288, https://doi.org/10.1038/s43247-022-00618-z, 2022b.

Sellitto, P., Belhadji, R., Cuesta, J., Podglajen, A., and Legras, B.: Radiative impacts of the Australian bushfires 2019–2020 – Part 2: Large-scale and in-vortex radiative heating, Atmos. Chem. Phys., 23, 15523–15535, https://doi.org/10.5194/acp-23-15523-2023, 2023.

Sellitto, P., Siddans, R., Belhadji, R., Carboni, E., Legras, B., Podglajen, A., Duchamp, C., and Kerridge, B.: Observing the SO_2 and sulfate aerosol plumes from the 2022 Hunga eruption with the Infrared Atmospheric Sounding Interferometer (IASI), Geophys. Res. Lett., 51, e2023GL105565, https://doi.org/10.1029/2023GL105565, 2024.

Taha, G., Loughman, R., Colarco, P. R., Zhu, T., Thomason, L. W., and Jaross, G.: Tracking the 2022 Hunga Tonga-Hunga Ha'apai aerosol cloud in the upper and middle stratosphere using space-based observations, Geophys. Res. Lett., 49, e2022GL100091, https://doi.org/10.1029/2022GL100091, 2022.

van de Hulst, H.: Light Scattering by Small Particles, Dover Books on Physics Series, Dover Publications, Mineola, New York, USA, https://books.google.fr/books/about/Light_Scattering_by_Small_Particles.html?id=6ivW_TgIdjIC&redir_esc=y (last access: 18 June 2025), 1957.

Vömel, H., Evan, S., and Tully, M.: Water vapor injection into the stratosphere by Hunga Tonga-Hunga Ha'apai, Science, 377, 1444–1447, https://doi.org/10.1126/science.abq2299, 2022.

Wrana, F., von Savigny, C., Zalach, J., and Thomason, L. W.: Retrieval of stratospheric aerosol size distribution parameters using satellite solar occultation measurements at three wavelengths, Atmos. Meas. Tech., 14, 2345–2357, https://doi.org/10.5194/amt-14-2345-2021, 2021.

Wrana, F., Niemeier, U., Thomason, L. W., Wallis, S., and von Savigny, C.: Stratospheric aerosol size reduction after volcanic eruptions, Atmos. Chem. Phys., 23, 9725–9743, https://doi.org/10.5194/acp-23-9725-2023, 2023.

Zhu, Y., Bardeen, C. G., Tilmes, S., Mills, M. J., Wang, X., Harvey, V. L., Taha, G., Kinnison, D., Portmann, R. W., Yu, P., Rosenlof, K. H., Avery, M., Kloss, C., Li, C., Glanville, A. S., Millán, L., Deshler, T., Krotkov, N., and Toon, O. B.: Perturbations in stratospheric aerosol evolution due to the water-rich plume of the 2022 Hunga-Tonga eruption, Commun. Earth Environ., 3, 248, https://doi.org/10.1038/s43247-022-00580-w, 2022.